PLOS ONE

Asymmetry in Signal Propagation between the Soma and Dendrites Plays a Key Role in Determining Dendritic Excitability in Motoneurons

Hojeong Kim[1,3]*, Kelvin E. Jones[2], C. J. Heckman[3,4,5]

1 Division of Robotics Research, Daegu Gyeongbuk Institute of Science & Technology, Daegu, Korea, 2 Centre for Neuroscience and Faculty of Physical Education and Recreation, University of Alberta, Edmonton, Canada, 3 Department of Physiology, Northwestern University Feinberg School of Medicine, Chicago, United States of America, 4 Department of Physical Medicine and Rehabilitation, Northwestern University Feinberg School of Medicine, Chicago, United States of America, 5 Department of Physical Therapy and Human Movement Science, Northwestern University Feinberg School of Medicine, Chicago, United States of America

Abstract

It is widely recognized that propagation of electrophysiological signals between the soma and dendrites of neurons differs depending on direction, i.e. it is asymmetric. How this asymmetry influences the activation of voltage-gated dendritic channels, and consequent neuronal behavior, remains unclear. Based on the analysis of asymmetry in several types of motoneurons, we extended our previous methodology for reducing a fully reconstructed motoneuron model to a two-compartment representation that preserved asymmetric signal propagation. The reduced models accurately replicated the dendritic excitability and the dynamics of the anatomical model involving a persistent inward current (PIC) dispersed over the dendrites. The relationship between asymmetric signal propagation and dendritic excitability was investigated using the reduced models while varying the asymmetry in signal propagation between the soma and the dendrite with PIC density constant. We found that increases in signal attenuation from soma to dendrites *increased* the activation threshold of a PIC (hypo-excitability), whereas increases in signal attenuation from dendrites to soma *decreased* the activation threshold of a PIC (hyper-excitability). These effects were so strong that reversing the asymmetry in the soma-to-dendrite vs. dendrite-to-soma attenuation, reversed the correlation between PIC threshold and distance of this current source from the soma. We propose the tight relation of the asymmetric signal propagation to the input resistance in the dendrites as a mechanism underlying the influence of the asymmetric signal propagation on the dendritic excitability. All these results emphasize the importance of maintaining the physiological asymmetry in dendritic signaling not only for normal function of the cells but also for biophysically realistic simulations of dendritic excitability.

Competing Interests: Kelvin E Jones, who is a co-author of this manuscript, is a PLOS ONE Editorial Board member. There are no patents, products in development or marketed products to declare. This does not alter the authors' adherence to all the PLOS ONE policies on sharing data and materials.

* E-mail: hojeong.kim03@gmail.com

Introduction

Many neurons in the central nervous system have voltage gated ion channels (VGICs) in their dendrites. The activation of dendritic VGICs is location sensitive, leading to functional impacts on dendritic signaling and firing patterns [1–4]. Therefore, an accurate understanding of the influence of the dendritic structure on the activation of dendritic VGICs is needed. In other words, dendritic structure influences not only the passive excitability of dendrites but also their "active" excitability (here we use the phrase "dendritic excitability" to refer primarily to the active component involving dendritic VGICs).

The activation properties of dendritic VGICs were initially investigated using voltage or current clamp at the cell body [5]. Since a command signal (voltage or current) applied to the soma attenuates along the path of the dendritic trees, due to their cable properties [6], higher command signals are required to activate more distal VGICs. This effect gives rise to space-clamp as a potential confounding factor for interpretation of dendritic

excitability [7,8]. Many studies using neuron models accounted for this confounding factor by characterizing the degree of signal attenuation from the soma to the dendrites, e.g. using a coupling conductance, as the key determinant for the location dependence of VGIC activation [9–11].

However, studies focused on dendritic anatomy have demonstrated a more complex signal attenuation process exists between the soma and dendrites. Both experimental evidence [12] and computational analyses [13,14] have emphasized that the attenuation of electrical signals in dendrites is asymmetric with respect to propagation *direction* (i.e. soma to dendrites and vice versa), and is moderated by *frequency* (direct (DC) or alternating (AC) current). This direction and frequency dependent dendritic signaling has been analyzed using two-port circuit theory [15] and morphoelectrotonic transformation of the anatomy of dendrites [16]. These studies suggested that a theoretical examination and understanding of dendritic excitability should go beyond the previous qualitative, or phenomenological, representation of DC signal attenuation from the soma to the dendrites. Furthermore, the

previous analysis of dendritic signaling between the soma and a single point in the dendrites (i.e. point-to-point) should be extended to reflect more natural conditions in which the VGICs or synaptic inputs are positioned on many dendrites.

To systematically investigate the relationship between the complex signaling properties and dendritic excitability, the independent modulation of individual signaling properties is necessary which has been known to be very difficult in the anatomically reconstructed models. Thus, a reduced modeling approach has been developed in the 'point-to-point' condition between the soma and dendrites for theoretical purposes in our previous studies [17,18]. However, it has not been validated whether the theoretical reduced models would be appropriate for the 'point-to-all' condition between the soma and dendrites where the VGICs or synaptic inputs are distributed in all dendritic branches over the limited range of the distance from the soma and may reproduce the input-output properties of the corresponding full model with realistic membrane excitability (i.e. Hodgkin-Huxley type) in both passive and active states.

Here we first compare the dependency of dendritic signaling on the direction and frequency among different types of spinal motoneurons in the point-to-all condition. Based on the consistent characteristics of this asymmetry across motoneuron types, we then chose one of these types in the motoneurons to provide the basis for validation of the reduced modeling approach that allows us to systematically examine the influence of the direction and frequency dependent dendritic signaling, to identify the relationship between asymmetric signal propagation and dendritic excitability. Specifically we elucidate whether the complex signaling properties of the dendrites are essential to physiologically represent dendritic excitability and how changes in these signaling properties affect normal patterns of activation of voltage sensitive channels in the dendritic tree.

Methods and Materials

Preparation of motoneuron anatomy

The morphological data of six type-identified cat spinal α-motoneurons (Vemoto1-6 in Burke's Lab.) was downloaded from http://NeuroMorpho.Org [19] and translated into the NEURON simulation environment v 6.1.1 using Import3D tool [20]. For individual imported motoneurons, the initial segment/axonal hillock was added to the soma after correcting the size of the cell body to the dimension previously reported [21,22].

Assignment of passive membrane properties

The values for the specific membrane resistivity (R_m) were assigned to the five motoneurons (Vemoto1-4 and 6) as previously reported and used in computer simulations [21,23,24]. The electrotonic properties for the five motoneurons were fully addressed in our previous study [21], assuming uniform cytoplasmic resistivity ($R_a = 70$ $\Omega\cdot$cm) and specific membrane capacitance ($C_m = 1$ μF/cm^2) [23]. Our initial simulations with the five anatomical motoneuron models (Vemoto1–4 and 6) used non-uniform R_m much lower at the soma compared to the dendrites considering the impalement resulting from sharp electrodes at the soma (i.e. somatic shunt effect) [25–27]. To approximate the presumed non-impaled in vivo condition, in later simulations for all six anatomical models we used a uniform R_m chosen to give a desired value of input resistant at the soma.

## Generation of voltage attenuation curve and voltage decay constant

The voltage attenuation (VA) factor representing signal propagation of the dendrites was defined as a ratio of voltage at the measurement site to voltage at the current injection site in the passive membrane condition [14,15]. Both direct (DC) and alternating current (AC) were taken into account for physiological current components flowing between the soma and the dendrites: DC for steady current stimulation at the soma, tonic synaptic inputs, persistent currents at the dendrites, and AC for action potentials at the soma. Three VA factors, two for the somatofugal direction with somatically injected DC (VA_{SD}^{DC}) and 250 Hz-AC (VA_{SD}^{AC}) input and one (VA_{DS}^{DC}) for the somatocentric direction with simultaneous DC inputs to all points in the dendrites at the same distance from the soma, were calculated in the passive dendrites of the anatomically reconstructed neurons using the Impedance class tools in NEURON software [20]. The VA_{DS}^{DC} was measured specifically for the propagation of steady synaptic inputs and persistent inward current generated by VGICs that are distributed over all branches of the dendrites at the same distance from the soma. The amount of current injection for the VA_{DS}^{DC} was differentially supplied to individual points in the dendrites in proportion to the surface area of dendritic segment where each point was involved. The AC frequency of 250 Hz was calculated from the average spike width of 2 ms (or period $= 4$ ms) for motoneurons [28]. The VA_{SD}^{AC} for the AC signals with lower frequencies (<250 Hz) has been shown to be well conserved in our reduced modeling framework [18]. The individual VA data was plotted as a function of path length (i.e. D_{path}) from the soma. To quantify the rate of attenuation with the distance, the VA_{SD}^{DC} and VA_{SD}^{AC} were fitted by single exponential function with voltage decay constant (λ_{SD}^{DC} and λ_{SD}^{AC}) [18,21]. A Boltzmann equation was arbitrarily chosen and modified to best fit the inverse-sigmoid shape of VA_{DS}^{DC} data in a wide range (0.4–4.0 MΩ) of the input resistance at the soma. Using the modified Boltzmann equation, the overall profile of the VA_{DS}^{DC} was characterized with two parameters (α_1 and α_2) where α_1 approximately represents the distance at the $VA_{DS}^{DC} = 0.5$ and α_2 indicates the variation in the slope of the VA_{DS}^{DC} curve at α_1 (see Figure 1 for detailed shape). The α_1 and α_2 were also used in analyzing the dependency of the VA_{DS}^{DC} on the motoneuron types over the full range of somatic input resistance (0.4–4.0 MΩ). The parameter values of individual fitting equations were determined using the nonlinear regression function (i.e. nlinfit) in MATLAB.

$$VA_{SD}^{DC}(D_{path}) = \exp\left(-\frac{D_{path}}{\lambda_{SD}^{DC}}\right) \quad (1)$$

$$VA_{SD}^{AC}(D_{path}) = \exp\left(-\frac{D_{path}}{\lambda_{SD}^{AC}}\right) \quad (2)$$

$$VA_{DS}^{DC}(D_{path}) = \frac{1}{1 - \exp\left(\frac{-\alpha_1}{\alpha_2}\right) + \exp\left(\frac{D_{path} - \alpha_1}{\alpha_2}\right)} \quad (3)$$

The four voltage decay constants (λ_{SD}^{DC}, λ_{SD}^{AC} and α_1 & α_2 in equation (1) – (3)) specified for Vemoto6 were used to determine the values of three VA factors for the reduced models. The default values of the VA factors for the reduced model were specified at
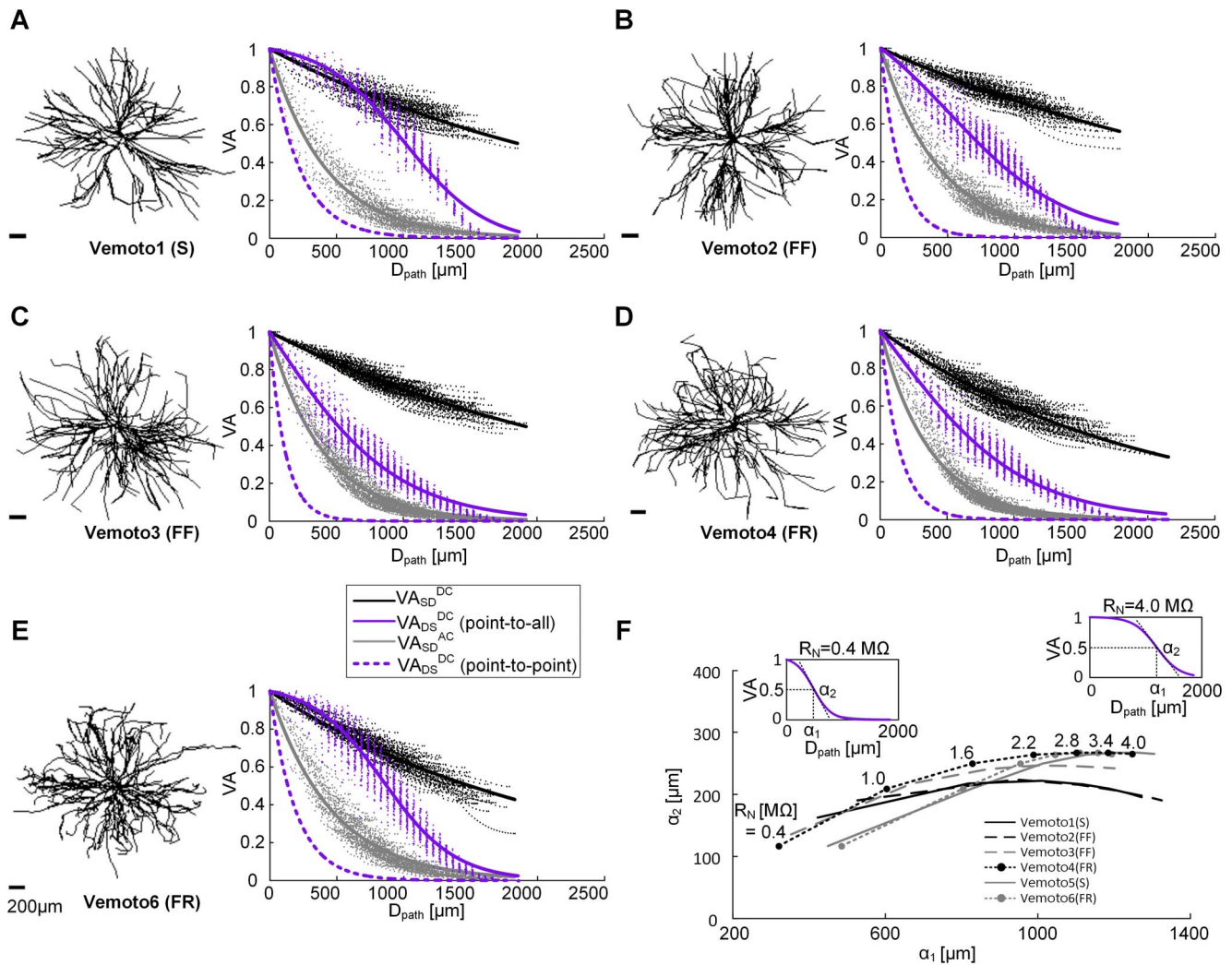
Figure 1. Characterization of voltage attenuation property of the dendrites. (**A**) – (**E**). Morphologies of the motoneurons in the left column and the three voltage attenuation (VA) factors measured at all distances (D_{path}) from the soma (VA_{SD}^{DC} in black, VA_{SD}^{AC} in gray and VA_{DS}^{DC} in purple) in the right column. A single exponential function ($exp(-D_{path}/\lambda)$) was used to fit the VA_{SD}^{DC} ($\lambda = 2678.7, 3085.6, 2763.7, 1945.5$ and 2156.4 for **A–E**) and VA_{SD}^{AC} ($\lambda = 420.1, 437.1, 402.3, 373.1$ and 464.7 for **A–E**), and a modified Boltzmann equation ($1/[1-exp(-\alpha_1/\alpha_2)+exp((D_{path}-\alpha_1)/\alpha_2)]$) for VA_{DS}^{DC} (α_1 & $\alpha_2 = 1020.8\&307.7, 635.2\&439.5, 327.9\&469.6, 374.2\&504.8$ and $861.9\&268.3$ for **A–E**). Note that purple solid lines represents the VA_{DS}^{DC} between the soma and all points in the dendrites at the same distance (i.e. point-to-all) whereas purple dotted lines ($exp(-D_{path}/\lambda)$ where $\lambda = 225, 143.6, 118.5, 144, 193.7$ for **A–E**) for the VA_{DS}^{DC} between the soma and a single point along the path of all individual dendritic trees from the soma (i.e. point-to-point). (**F**). The VA_{DS}^{DC} was measured in six type identified anatomically reconstructed motoneurons while varying the input resistance (R_N) from 0.4 to 4.0 MΩ. The α_1 (the distance at which the VA_{DS}^{DC} dropped to 50%) parameter was more sensitive to changes in R_N compared with α_2 parameter (a measure of the slope of the curve at α_1). The insets show examples of the VA_{DS}^{DC} curves at extreme R_N values of 0.4 and 4.0 MΩ. Note that the distribution of points (α_1, α_2) at the same R_N is not type specific (e.g. gray and black filled circles for FR-type motoneurons). S, FR and FF indicate slow twitch, fast twitch and fatigue resistant, and fast twitch and fast fatigable motoneuron type respectively.
doi:10.1371/journal.pone.0095454.g001

the D_{path} of 600 μm, which is an average of the distance interval (300–850 μm) previously reported for the distribution of PIC channels to produce experimentally observed nonlinear firing patterns in the anatomical model [29,30].

Reduced neuron model

A conductance-based, two-compartmental neuron model is used consisting of a somatic compartment and a dendritic compartment that are coupled with a single conductance. The passive dynamics of the reduced neuron model is determined by the five cable parameters: two conductances ($G_{m,S}$ and $G_{m,D}$) for the soma and dendrite, two capacitances ($C_{m,S}$ and $C_{m,D}$) for the

soma and dendrite, and one coupling conductance (G_C) between the soma and dendrite. The unique feature of our reduce modeling approach is that all five cable parameters of the reduced model are analytically determined from the five system properties (somatic input resistance (R_N), membrane time constant (τ_m), $VA_{SD}^{DC}(D_{path})$, $VA_{SD}^{AC}(D_{path})$ and $VA_{DS}^{DC}(D_{path})$) empirically measurable from real cells (see [18,21] for details of model equations and the derivation of inverse equations for the five system properties). The five passive parameters of the reduced model were uniquely determined for the VA factors specified at the distance from the soma by solving the inverse equations,

$$G_{m,S} = \frac{1 - VA_{DS}{}^{DC}}{r_N\left(1 - VA_{SD}{}^{DC}VA_{DS}{}^{DC}\right)} \qquad (4)$$

$$G_{m,D} = \frac{pVA_{DS}{}^{DC}\left(1 - VA_{SD}{}^{DC}\right)}{(1-p)r_N VA_{SD}{}^{DC}\left(1 - VA_{SD}{}^{DC}VA_{DS}{}^{DC}\right)} \qquad (5)$$

$$G_C = \frac{pVA_{DS}{}^{DC}}{r_N\left(1 - VA_{SD}{}^{DC}VA_{DS}{}^{DC}\right)} \qquad (6)$$

$$C_{m,D} = \frac{1}{\omega^{1-p}}\sqrt{\frac{G_C{}^2}{\left(VA_{SD}{}^{AC}\right)^2} - \left\{G_C + G_{m,D}(1-p)\right\}^2} \qquad (7)$$

$$\qquad (8)$$

$$C_{m,S} = \frac{\tau_m\{p(1-p)\tau_m G_{m,S}G_{m,D} + pG_{m,S}(\tau_m G_C - C_{m,D}) + P^2 G_{m,S}C_{m,D} + (1-p)(\tau_m G_C G_{m,D} - G_C C_{m,D})\}}{p\{(1-p)(\tau_m G_{m,D} - C_{m,D}) + \tau_m G_C\}}$$

where r_N is the input resistance (R_N) normalized with the surface area of the somatic compartment; ω is the maximum frequency component in an action potential; p is the ratio of somatic to total surface area of the reduced model. In the present study, the somatic surface area (315759.2 μm^2) of the reduced model represents total accumulated surface area from the soma up to $D_{path} = 600$ μm in the anatomically reconstructed motoneuron (i.e. Vemoto6). The r_N and p were calculated from the R_N (1.29 MΩ) and total surface area (641786.9 μm^2) of the Vemoto6. The default values of r_N (0.407 $\Omega \cdot m^2$), τ_m (7.2 ms), p (0.492), and ω ($2\pi \times 250$ Hz calculated from the period of 4 ms assuming the spike width of 2 ms) were set to be constant at all distances (i.e. D_{path}) for all reduced models used in the present study. The system equations and derivations of forward/inverse equations for the reduced model have been fully addressed in our previous studies.

Assignment of active membrane properties

A fast twitch and fatigue resistant (FR)-type motoneuron (Vemoto6) of six anatomical models was chosen for the comparison with the reduced model. The input-output properties of the Vemoto6 has been fully analyzed in the previous study with realistic types, kinetics and distribution of voltage-gated ion channels including slowly activated, long lasting L-type Ca PIC channels in many dendrites over the limited range (i.e. 300–850 μm) of the distance from the soma [29]. The same types and kinetics of voltage gated ion channels and excitatory synapse were used for both the anatomical and reduced motoneuron model (see Appendix in [29] for details of equations and parameter values). Briefly, action potentials were generated by various active currents: fast inactivating sodium current ($I_{Na,f}$), persistent sodium current ($I_{Na,p}$), delayed-rectifier potassium current ($I_{K,Dr}$), N-type calcium current ($I_{Ca,N}$), calcium dependent potassium current ($I_{K(Ca)}$) at the soma and $I_{Na,f}$, $I_{Na,p}$, $I_{K,Dr}$ at the initial segment/axonal hillock in the anatomical model, and $I_{Na,f}$, $I_{Na,p}$, $I_{K,Dr}$, $I_{Ca,N}$, $I_{K(Ca)}$ at the somatic compartment of the reduced model. Plateau potentials were produced by currents ($I_{Ca,L}$) mediated by L-type Ca^{2+} channels in the dendrites of both models. In the absence of the $I_{Ca,L}$, the active channel densities ($G_{Na,f}$ [mS/cm^2], $G_{Na,p}$ [mS/cm^2], $G_{K,Dr}$ [mS/cm^2], $G_{Ca,N}$ [mS/cm^2] and $G_{K(Ca)}$

[mS/cm^2]) responsible for spike generation were adjusted in both models to match the same height (i.e. 92.3 mV) of an action potential and afterhyperpolarization (AHP) properties (i.e. duration of 98.5 ms and depth of 3.1 mV) at the same rheobase current (i.e. 10.5 nA) that have been experimentally investigated without monoaminergic inputs to the motoneurons [31]. $G_{Ca,L}$ [mS/cm^2] for $I_{Ca,L}$ in the dendrite of the reduced model was determined to fit the peak current (i.e. -22 nA) measured in the anatomical model during triangular voltage clamp simulations while blocking all active currents at the soma [32].

Stimulation protocols

The voltage attenuation properties of the dendrites were characterized in the passive membrane condition with DC input (amplitude of 1 nA) for the $VA_{SD}{}^{DC}$ and the $VA_{DS}{}^{DC}$, and AC input (amplitude of 2 nA with frequency of 250 Hz) for the $VA_{SD}{}^{AC}$. The somatic input-somatic output relation was evaluated including the active membrane properties while applying slowly ascending and descending voltage (duration of 20 sec with peak of 30 mV starting from -70 mV) and current (duration of 10 sec with peak of 20 nA starting from 0 nA) clamp to the soma. To investigate the synaptic input-somatic output relation over a wide input range, the maximum conductance (i.e. G_{syn}) of excitatory synaptic receptors in the dendrites was varied in a slowly increasing and decreasing triangular form (duration of 20 sec with peak of 1.2 mS/cm^2 for the anatomical and 0.12 mS/cm^2 for the reduced case starting from 0 mS/cm^2). The peak of the G_{syn} in the reduced case was adjusted to match the same onset timing (5 ms) and peak value (-13.6 mV) of the plateau potential as the anatomical case. The smaller G_{syn} in the reduced case resulted from the larger surface area of the dendrite for Ca PIC channels compared to the anatomical case.

Results

Three voltage attenuation parameters to characterize dendritic signaling in neurons

Signal propagation of the dendrites was characterized in fully reconstructed motoneuron (MN) models by three voltage attenuation (VA) factors: two for the soma-to-dendrite direction with DC ($VA_{SD}{}^{DC}$) and AC ($VA_{SD}{}^{AC}$) input to the soma, and one ($VA_{DS}{}^{DC}$) for the dendrite-to-soma direction with simultaneous DC inputs to all points in the dendrites at the same distance from the soma. The three VA factors define neuron voltage profiles in response to steady current injected at the soma ($VA_{SD}{}^{DC}$), action potentials propagating from the initial segment and soma into the dendrites ($VA_{SD}{}^{AC}$), and steady synaptic inputs and plateau potential generated by VGICs in the dendrites ($VA_{DS}{}^{DC}$).

Figure 1(**A–E**) shows voltage attenuation as a function of distance from the soma (D_{path}) in the five (i.e. Vemoto1–4 and 6) type-identified anatomically reconstructed spinal MNs. Each point in this figure shows the voltage attenuation at a single point in a dendritic branch at the indicated path distance. In all five anatomical MN models, the spatial profile of the individual VA factors was distinguishably different indicating the direction and frequency dependency of the dendritic signaling. The different dependencies of individual VA factors on the distance stem from the unbalance in electrical load between the soma and dendrites due to the highly branching structure of the dendrites and the low-pass filtering effect due to the cable properties. The vertical alignment of the data for the $VA_{DS}{}^{DC}$ results from spatial sampling at a resolution of 50 μm. The $VA_{DS}{}^{DC}$ data were fit to an inverse sigmoid curve (solid purple lines in Figure 1(**A**) and 1(**E**)), rather than the single-exponential curve (dashed purple line)

previously fit to VA_{DS}^{DC} when this parameter was computed between the soma and a *single* point in the dendrites [21]. The difference in DC voltage attenuation from the dendrites to the soma when calculated with the new approach was obvious in all five anatomical MN models and resulted from the summation of multiple inputs at the soma originating from the separate dendritic branches. The data from the other two voltage attenuation parameters were well fit by single exponential curves, as previously reported [18,21]. The equations fitting individual VA data were used to calculate the values of three VA factors for the reduced MN models.

The spatial profile of the two VA factors from the soma to the dendrites was consistent across different types (slow twitch (S), fast twitch and fatigue-resistible (FR), fast twitch and fatigable (FF)) of MN models whereas the VA factor from the dendrites to the soma appeared to be related to the MN types. The S- or FR-type MN model with high input resistance (e.g. Vemoto1 (1.9 MΩ) or Vemoto6 (1.25 MΩ)) tended to be much more slowly attenuated with the distance showing the inverse sigmoid profile compared to the FF- or FR-type MN models with low input resistance (e.g. Vemoto2–3 (0.7–0.8 MΩ) or Vemoto4 (0.97 MΩ)).

Thus, we further analyzed six type-identified anatomically reconstructed MNs to evaluate how VA_{DS}^{DC} generalized to a population of MNs with widely varying morphological and electrical characteristics (Figure 1(**F**)). We changed the specific membrane resistivity so that all anatomical models had the same input resistance (R_N) at the soma, and recalculated and fit the VA_{DS}^{DC} data to the inverse sigmoid curve to find the coefficients α_1 and α_2. The α_1 parameter was more sensitive to changes in R_N compared with α_2 parameter. All six MN morphologies had similar relationships between R_N and changes in α_1 & α_2 suggesting that the differences in morphology of the 6 models did not play a major role in VA_{DS}^{DC} behavior. The evaluation of VA_{SD}^{DC} and VA_{SD}^{AC} for a population of MNs was presented in our previous studies [18,21].

All these results suggest that the voltage attenuation properties in the motoneurons might not be specific to the type-related morphology of motoneurons, but a generic property of the branched architecture of dendritic trees.

Reduced motoneuron model incorporating VA factors for dendritic excitability

One (FR-type, Vemoto6) of the anatomical MN models was chosen for our evaluation of the relationship between the signal attenuation properties and dendritic excitability since the anatomical model has been fully analyzed in the previous studies [29,33] for the influence of dendritic PICs on MN firing patterns and synaptic integration that have been observed in various species including turtle [34], rat [35], mouse [36] and cat [37].

To explicitly evaluate the influence of the three VA factors on the location dependence of dendritic excitability, the anatomically reconstructed MN (i.e. Vemoto6) was reduced using our recently developed two-compartment model that analytically retained the VA factors of its original cell as well as whole cell properties measured at the soma such as input resistance (R_N) and system time constant (τ_m) [18] (Figure 2(**A**)). For the validation of the reduced model in physiological realism, the systematic comparison between the full anatomical model and the reduced model was conducted in two steps. Firstly, all levels of input/output relations were compared at $D_{path} = 600$ μm with respect to: the passive membrane properties, the dendritic excitability with PIC channels in the dendrites, and the cellular excitability for firing output at the soma. Then, we constructed multiple two-compartment models

and matched their excitability for D_{path} values along the dendrites of the full model.

Comparison of passive dynamics of the reduced and full models. The five system parameters (i.e. R_N, τ_m, and VA_{SD}^{DC}, VA_{DS}^{DC} and VA_{SD}^{AC} for $D_{path} = 600$ μm) used to solve for the passive properties of the reduced model, were sufficient to replicate the desired passive membrane features of the anatomical model (Figure 2(**B**) & (**C**)). The time course of depolarization and repolarization in response to the long lasting step current at the soma was very similar in both cases (Figure 2(**B**)), despite the slight difference in the second time constant (or equalizing time constant, τ_1 in Figure 2(**C**)). To avoid the overlap of lines due to the same input resistance between the anatomical and reduced model, brief current pulse with smaller amplitude was applied to the soma for the anatomical (blue) than reduced (red) case resulting in the downward shift of the voltage response for the anatomical case in Figure 2(**C**). The somatic and dendritic membrane potentials measured for the calculation of VA_{SD}^{DC} were identical, whereas those for the VA_{DS}^{DC} were slightly larger by about 0.09% in the reduced model compared to the anatomical model at steady state (Figure 2(**D**)). The similarity of dendritic depolarization in the two models, by the same dendritically injected current, indicates that the input resistance at the dendrite of the reduced model captures the input resistance of the complex dendritic network of the anatomical model at the $D_{path} = 600$ μm. The amplitude ratio (i.e. VA_{SD}^{AC}) between somatic and dendritic membrane potential in response to 250 Hz-AC input to the soma was the same between two models (Figure 2(**E**)).

Comparison of dendritic PIC activation. The next comparison was for dendritic PIC activation during either slow-ramp voltage or current clamp applied to the soma, while blocking all active currents generated at the soma. In this way, we could isolate the influence of the DC signal attenuation (i.e. VA_{SD}^{DC} and VA_{DS}^{DC}) on the PIC activation from that of the AC signal attenuation (i.e. VA_{SD}^{AC}). The maximum conductance of the Ca channels in the dendrite of the reduced model was fit to the peak current measured in the anatomical model during triangular voltage clamp simulations ($I_{PIC,Peak}$ in Figure 2(**F**)). During the rising phase of triangular voltage clamp the two models produced similar N-shaped dynamics of the total current (I_{Total}, top panel in Figure 2(**F**)). The consequence of PIC activation was a long lasting depolarization (plateau potential, top panel in Figure 2(**G**)) at both soma and dendrites during the triangular current stimulation to the soma. The delayed offset of the PIC during the falling phase of voltage clamp relative to the rising phase of voltage clamp resulted in hysteresis of the current/voltage relationships (bottom panels in Figure 2(**F**) & (**G**)). A difference between the two models was the earlier onset and slower offset of the PIC in the anatomical dendrites, probably due to the variance in the input resistance of individual dendritic branches at the D_{path} of 600 μm. However, this difference was negligible in current clamp conditions during activation of the plateau potential (Figure 2(**G**)).

Comparison of firing responses. Because the activation of PIC channels in the dendrites is influenced by action potentials propagating into the dendrites [18], we compared firing patterns in response to the triangular current stimulation to the soma between the anatomical and reduced models. In the presence of Ca PIC channels, the two models showed similar nonlinear firing behavior (bottom panel in Figure 2(**H**)), i.e. counter-clockwise hysteretic frequency-current (F-I_{soma}) relationship with sustained firing below the current threshold for spike initiation. The firing rate at the end of the descending phase of the current injection is greater for the anatomical model because the slower offset of the PIC results in more inward current. Overall there was a good
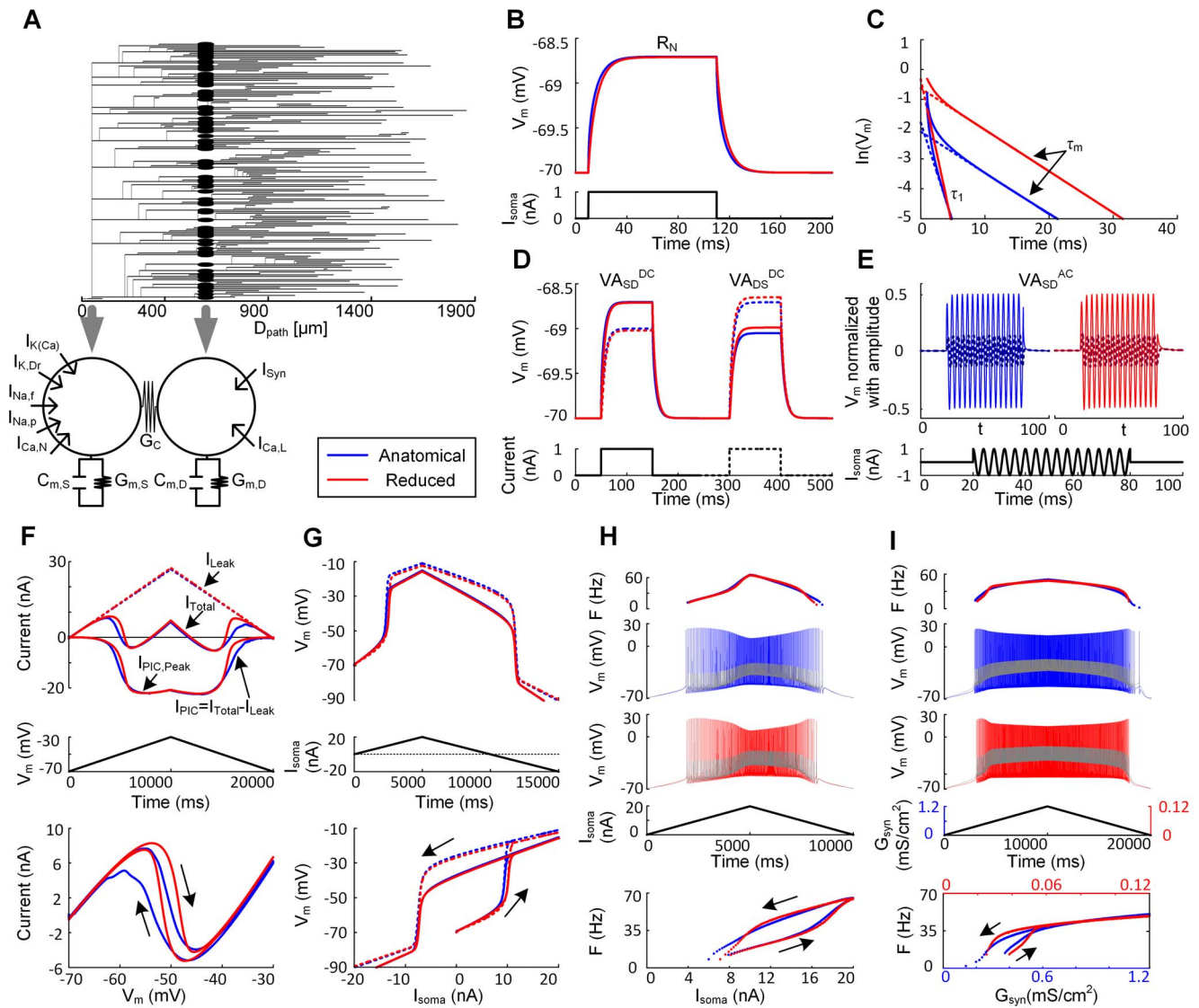
Figure 2. Comparison of the anatomical (blue) and reduced (red) MN model. (A). Reduction of anatomical dendrites. A dendrogram (upper panel) of a MN (i.e. vemoto6 in Methods) with path length (D_{path}) from the soma and two compartments (bottom panel) of the reduced model representing the soma/initial segment/axonal hillock (indicated by left arrow) and all points in the narrow band (e.g. mean of 600 μm and standard deviation of 4 μm, right arrow) of dendrites of its original cell. Note that membrane potentials at individual points in the dendrites of the anatomical model were averaged for the purpose of comparison to the reduced model. **(B)** – **(E)**. Passive dynamics. All five passive parameters ($G_{m,S} = 0.143$ mS/cm^2, $G_{m,D} = 0.131$ mS/cm^2, $C_{m,S} = 1.058$ μF/cm^2, $C_{m,D} = 0.915$ μF/cm^2, $G_C = 0.211$ mS/cm^2) of the reduced model were analytically determined to retain the five system properties measured from the anatomical model: input resistance ($R_N = 1.29$ MΩ) and membrane time constant ($\tau_m = 7.2$ ms) obtained by peeling analysis at the soma, and three voltage attenuation factors ($VA_{SD}^{DC} = 0.76$, $VA_{DS}^{DC} = 0.75$, $VA_{SD}^{AC} = 0.27$) at $D_{path} = 600$ μm. **(B)**. Time course of membrane potential (V_m) in response to the step current (I_{soma}) injected to the soma for calculating R_N. **(C)**. The semilog plot (solid lines) of transient voltage response at the soma to brief current pulse with smaller amplitude for anatomical than reduced case for τ_m and τ_1 (equalizing time constant) equivalent to the inverse of slope of linear regression (dotted) line fitting the tail of each curve. **(D)**. Time courses of V_m for VA_{SD}^{DC} from the soma (solid lines) to dendrites (dotted lines) and VA_{DS}^{DC} in the opposite direction, in response to DC input (bottom panel) to the soma (solid line) and dendrites (dotted line). **(E)**. Time course of V_m normalized with its amplitude for VA_{SD}^{AC} from the soma (solid line) to dendrites (dotted line), in response to somatically injected AC current (I_{soma}) with the frequency of 250 Hz. **(F)**, **(G)**. PIC activation with the addition of $I_{Ca,L}$ to the dendrites of both models. **(F)**. Time course of effective PIC (I_{PIC}, upper panel) obtained by subtracting leak (I_{Leak}) from total current (I_{Total}) injected for following the triangular voltage-clamp (V_m, middle panel) at the soma, and I_{Total}-V_m relationship (bottom panel). **(G)**. Time course of V_m (upper panel) at the soma (solid lines) and dendrites (dotted lines) in response to triangular current clamp at the soma (I_{soma}, middle panel), and V_m-I_{soma} relationship (bottom panel). Arrows indicate the ascending and descending phase of triangular voltage and current clamp. Maximum conductance ($G_{Ca,L}$) for $I_{Ca,L}$ was 1.37 mS/cm^2 for the anatomical and 0.124 mS/cm^2 for the reduced case. **(H)**, **(I)**. Cellular excitability with the addition of $I_{Na,f}$, $I_{Na,p}$, $I_{K,Dr}$, $I_{Ca,N}$ and $I_{K(Ca)}$ to the soma of both models. **(H)**. Instantaneous firing rates (F, upper panel), time course of V_m (blue & red for the soma, and gray for the dendrite) in response to triangular current stimulation (I_{soma}) to the soma, and F-I_{soma} curve (bottom panel). Maximum conductances for the active currents in the anatomical case were $G_{Na,f} = 0.71$ [S/cm^2], $G_{K,Dr} = 0.23$ [S/cm^2], $G_{Ca,N} = 0.01$ [S/cm^2], $G_{K(Ca)} = 0.0258$ [S/cm^2] at the soma, $G_{Na,f} = 2.7$ [S/cm^2], $G_{Na,p} = 0.033*10^{-3}$ [S/cm^2], $G_{K,Dr} = 0.17$ [S/cm^2] at the initial segment and axon hillock, and $G_{Ca,L} = 1.37$ [mS/cm^2] in the dendrites. For the reduced model, $G_{Na,f} = 26.75$ [mS/cm^2], $G_{Na,p} = 0.00086$ [mS/cm^2], $G_{K,Dr} = 6.2$ [mS/cm^2], $G_{Ca,N} = 0.008$ [mS/cm^2], $G_{K(Ca)} = 0.54$ [mS/cm^2] at the soma and $G_{Ca,L} = 0.124$ [mS/cm^2] at the dendrite. **(I)**. F, V_m (blue & red for the soma, and gray for the dendrite) in response to triangular variation of the maximum conductance (G_{syn}) for the synaptic receptors positioned at all points at $D_{path} = 600$ μm, and F-G_{syn} curve. Arrows indicate the ascending and descending phase of G_{syn}.
doi:10.1371/journal.pone.0095454.g002

match of firing rate behavior in the two models. Figure 2(**I**) shows that the reduced model also matched the full model even in the case where tonic synaptic inputs interacted with PIC channels in the dendrites [38]. The amplitude of membrane potentials at the soma and dendrites was similar between the two models during the triangular changes in G_{syn}. Consistent with the F-I$_{soma}$ relationship with somatically injected current (bottom panel in Figure 2(**I**)), the anatomical model had the faster onset of the PIC channels and longer duration of sustained firing below the threshold for the spiking than the reduced model.

Comparison of the effects of varying the distance for PIC location. The above results only applied to the case where the PIC channels were localized at all points of the dendritic branches separated by about 600 microns away from the soma in both the full and reduced models (see Figure 2A for graphical description). We next varied the location of the ion channels that generate the PIC. For each location, a new two-compartment model was created and matched to the passive properties (R$_N$, τ_m and three VAs) of the anatomical model. This required location dependent alterations in the VA parameters of the reduced models. The PIC channel density of both models was adjusted to maintain a constant peak of I$_{PIC}$ determined at the D$_{path}$ = 600 μm [32]. In general, the reduced model was able to predict the overall firing pattern of the anatomical model at all distances from the soma during either somatic current stimulation or synaptic input (Figure 3). As the PIC channels moved towards the dendritic terminals, both threshold current and synaptic conductance for the activation of plateau potential decreased (gray arrows in Figure 3). These results indicate that the more distant the location of the PIC channels in the dendrites, the more ''excitable'' the cell is.

## Dependency of dendritic excitability on the VA factors

We have quantitatively characterized the voltage attenuation properties of the dendrites using the anatomically reconstructed MN models (Figure 1) and showed that physiological changes in the VA factors for the two- compartment models allowed representation of the spatial variation in the threshold for activating plateau potentials along the path of the complex MN dendrites (Figure 2 and 3). Therefore, we next used the realistic two-compartment models to systematically evaluate how the VA factors influence dendritic excitability. To achieve this, a sensitivity analysis of the effect of the VA factors on dendritic PIC activation was conducted for PIC channels located at different distances from the soma.

Sensitivity of cellular excitability to the VA factors. Triangular currents were injected at the soma to generate frequency-current (F-I$_{soma}$) curves and the threshold for PIC activation was estimated from the acceleration in firing. When VA$_{SD}^{DC}$ was decreased by 4.7% from its original value (0.76), a high threshold was detected at 19.8 nA and labeled I$_{S2}$ (Figure 4(**A**)). Similarly, when VA$_{SD}^{DC}$ was increased by 20.4%, a low current threshold for this acceleration was detected at 8.1 nA and labeled I$_{S1}$ (Figure 4(**B**)). A shift from I$_{S2}$, to I$_{S1}$ represents a hyperpolarizing shift of the threshold, indicating an increase in excitability. The sensitivity of each of the three voltage attenuation factors was inferred by measuring the amount of variation required to alter the acceleration in firing between I$_{S1}$ and I$_{S2}$. We inferred high sensitivity to a VA factor when small variations were required to achieve the target thresholds. The threshold for the firing acceleration was more sensitive to changes in the DC than AC VA factors (Figure 4(**E**)). Variation of the DC VA factors changed the threshold targets in opposite directions. Increasing the attenuation from the dendrites to the soma by decreasing VA$_{DS}^{DC}$ resulted in an increase in excitability. In
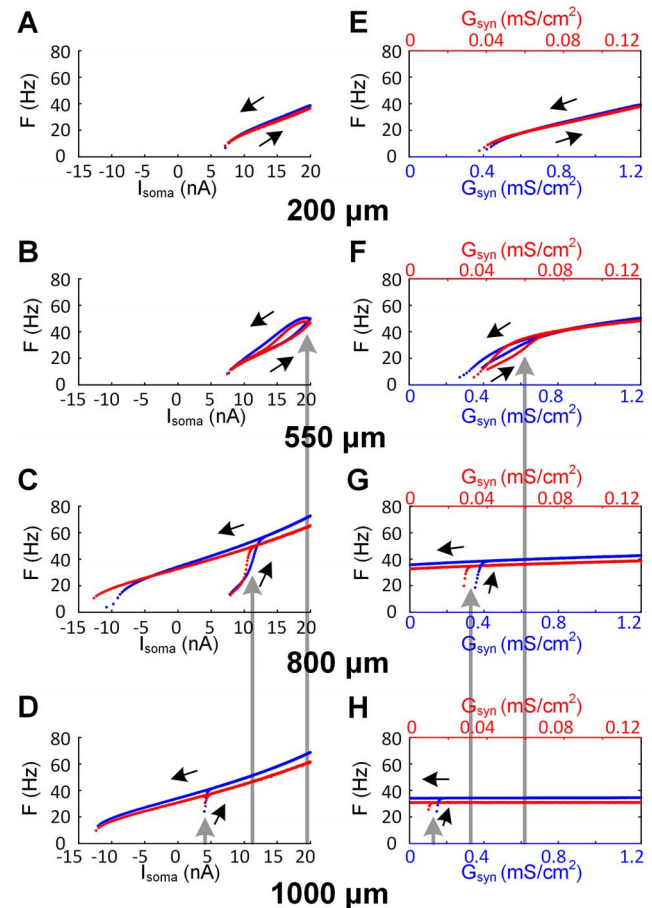
Figure 3. Cellular excitability of the anatomical (blue) and reduced (red) model with different locations of PIC channels in the dendrites. The neuron models and stimulation protocols were the same as those used in Figure 2(H) & (I) except for variation of PIC channel location in the dendrites. (A) – (D). Firing rates (F) in response to triangular current stimulation to the soma (I$_{soma}$). (E) – (H). Firing rates (F) in response to triangular variation of maximum conductance (G$_{syn}$) of excitatory synaptic receptors in the dendrites. The direction of black arrows indicates the ascending and descending phase of triangular current stimulation and change in G$_{syn}$. The gray arrows indicate the current and G$_{syn}$ threshold for activating plateau potentials at different distances from the soma. Note the negative relation between the distance and input threshold. At different locations in the dendrites, the three VA factors were VA$_{SD}^{DC}$ = {0.91, 0.77, 0.69, 0.63}, VA$_{DS}^{DC}$ = {0.96, 0.79, 0.57, 0.38} and VA$_{SD}^{AC}$ = {0.65, 0.31, 0.18, 0.12}; the density of Ca PIC channels were G$_{Ca,L}$ = {1.14, 1.27, 1.95, 4.1 mS/cm^2} in the anatomical and {0.11, 0.122, 0.132, 0.189 mS/cm^2} in the reduced model; the passive parameter values of the reduced model were G$_{m,S}$ = {0.078, 0.132, 0.174, 0.2 mS/cm^2}, G$_{m,D}$ = {0.179, 0.143, 0.1, 0.07 mS/cm^2}, G$_C$ = {0.918, 0.244, 0.114, 0.06 mS/cm^2}, C$_{m,S}$ = {0.609, 1.077, 1.211, 1.302 μF/cm^2}, C$_{m,D}$ = {1.239, 0.903, 0.764, 0.62 μF/cm^2}. Parameter values in the parentheses are in the order of increasing distance from 200 to 1000 μm.
doi:10.1371/journal.pone.0095454.g003

contrast, increasing the attenuation in the opposite direction, VA$_{SD}^{DC}$, produced a decrease in excitability. Therefore, we conclude that VA$_{SD}^{DC}$ is positively correlated, whereas VA$_{DS}^{DC}$ is negatively correlated with excitability (Figure 4(**F**)). The slope of the regression lines indicates that current threshold is most sensitive to voltage attenuation from the soma to the dendrites. The relatively modest effects of changes in VA$_{SD}^{AC}$ also increase excitability.
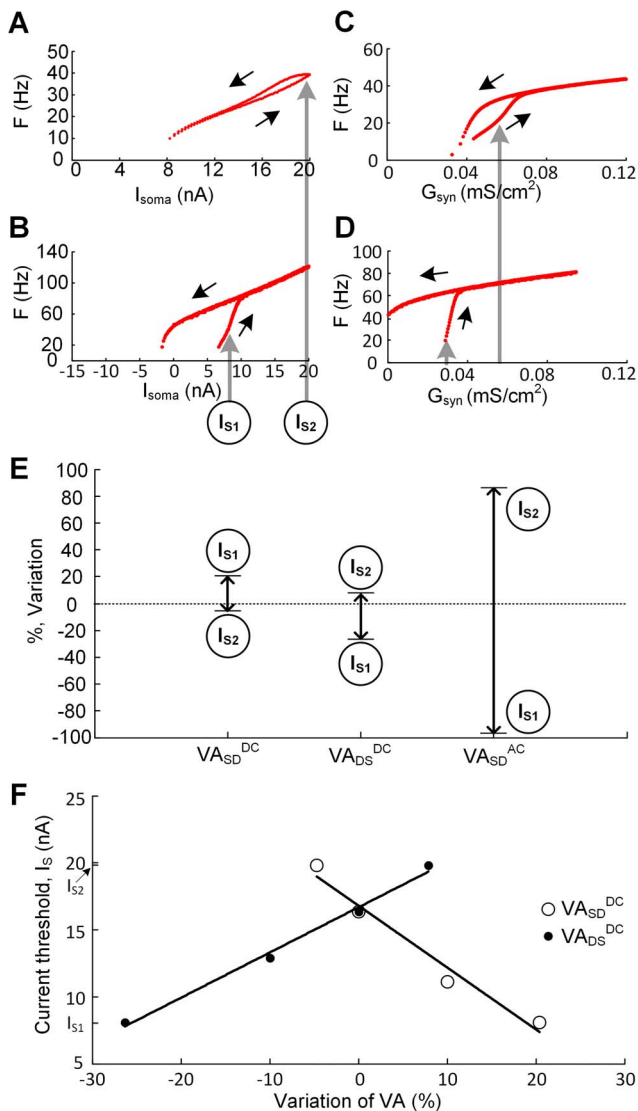
Figure 4. Sensitivity of cellular excitability to the VA factors. Using the same reduced model and ramp stimulation protocols used in Figure 2(**H**) & (**I**), F-I_{soma} and F-G_{syn} relationships were simulated while varying individual VA factors independently. (**A**), (**B**). F-I_{soma} curves with VA_{SD}^{DC} decreased by 4.7% and increased by 20.4% from its original value (0.76). Circled letters, I_{S1} (8.1 nA) and I_{S2} (19.8 nA), on vertical gray lines indicate decreased and increased current threshold for initiating firing acceleration as a result of changing the VA_{SD}^{DC}. Black arrows indicate the rising and falling phase of triangular current stimulation to the soma. (**C**), (**D**). F-G_{syn} curves with VA_{SD}^{DC} changed by the same variation (%) as applied to (**A**) and (**B**). Vertical gray arrows indicate increased (about 0.055 mS/cm^2, left column) and decreased (about 0.029 mS/cm^2, right column) threshold-G_{syn} for the firing acceleration as a result of varying the VA_{SD}^{DC}. Black arrows indicate the rising and falling phase of triangular change in G_{syn} at the dendrite. (**E**). The percent variation in individual VA factors (VA_{SD}^{DC}, VA_{DS}^{DC}, VA_{SD}^{AC}) to produce the firing acceleration at either I_{S1} or I_{S2}. 0% represents the original values of VA factors and minus sign in the ordinate indicates the decrease in VA factor values. (**F**). Relationship of threshold current (I_S) for the firing acceleration and the percent variation in DC VA factors. Data points were fitted to a linear regression line. Note that R_N for the reduced model was set to be 1.29 MΩ.
doi:10.1371/journal.pone.0095454.g004

Similar effects of varying individual voltage attenuation factors were found in the case where the PIC was activated by synaptic conductances applied to the dendrites (Figure 4(**C**) & (**D**)). The three voltage attenuation factors showed the same correlations with excitability to synaptic input as current input to the soma. That is, increases in VA_{SD}^{DC} increased excitability, whereas increases in VA_{DS}^{DC} or VA_{SD}^{AC} decreased excitability.

Role for the VA factors in the spatial profile of dendritic excitability. We next explored how the voltage attenuation factors affected the relationship between PIC location along the dendrites and its threshold for activation. When all three VA factors were constrained to biophysical values obtained from simulations with the anatomical MN model (Figure 1(**A**)), moving the PIC location close to the soma resulted in an increase in PIC activation threshold: the closer the PIC, the greater the current (either injected or synaptic) required to activate it (Figure 3). In the present analysis, we held VA_{SD}^{DC} at its physiological values for each PIC distance and varied VA_{DS}^{DC} and VA_{SD}^{AC}. The results of these changes were striking in that the spatial order of the PIC activation observed in the physiological case (Figure 3) could be inverted, as illustrated in Figure 5. That is, PIC threshold activation shifted to lower values as its location was moved closer to the soma. As a result, variations in VA_{DS}^{DC} and VA_{SD}^{AC} could be found to match the firing patterns when all three VA factors were constrained to their physiological ranges (Figure 3) with the PIC at non-physiological locations. For instance, the F-I_{soma} curve at $D_{path} = 1000$ μm in the physiological case (Figure 3(**D**) & (**H**)) could be reproduced at $D_{path} = 200$ μm by decreasing only the VA_{DS}^{DC} from 0.96 to 0.47 (Figure 5(**A**) & (**E**)), whereas the increase in both the VA_{DS}^{DC} (0.63→0.876) and VA_{SD}^{AC} (0.12→0.5) could lead to the same F-I_{soma} curve at $D_{path} = 200$ μm of the physiological case (Figure 3(**A**)) at $D_{path} = 1000$ μm (Figure 5(D)). The strong dependency of the PIC activation and associated firing patterns on the VA_{DC}^{DC} and VA_{SD}^{AC}, at all positions in the dendrites, indicates that all three voltage attenuation factors are necessary for biophysically realistic simulations of dendritic excitability.
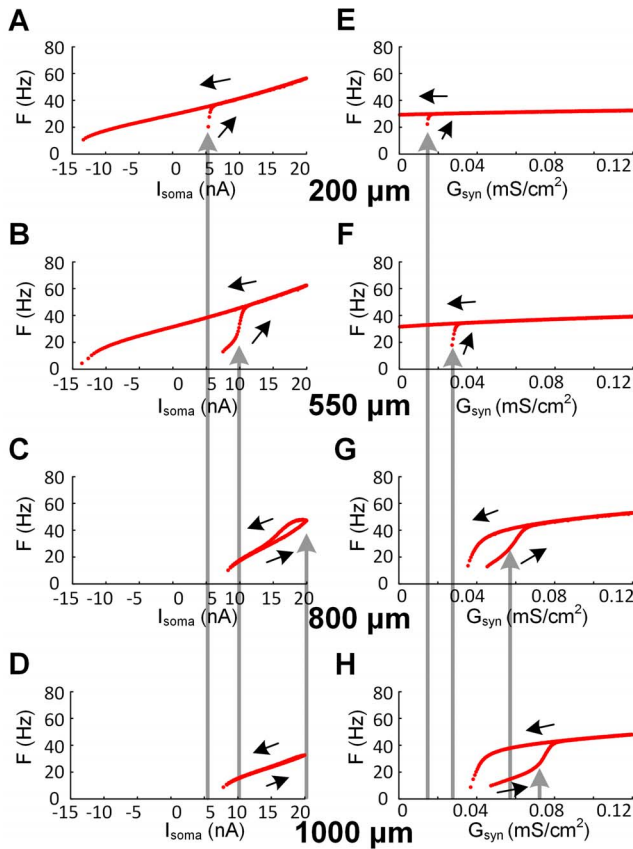
Discussion

The high dimensionality of dendritic systems has made it challenging to get insights into whether and how the complex (directional and frequency-dependent) dendritic signaling contributes to the activation of voltage gated ion channels in dendrites. We have demonstrated using realistically reduced MN models that the asymmetry in voltage attenuation between the soma and the dendrites plays an essential role in determining the spatial activation pattern of voltage sensitive dendritic channels and associated somatic firing output. Our results also showed that voltage attenuation properties in several different types of neurons have an asymmetric profile that is remarkably similar to that in spinal MNs, suggesting that the essential role of this asymmetry for normal function may apply widely in neurons. All these results support the conclusion that the biophysically based asymmetry in signal propagation of the dendrites should be maintained in reduced models of neurons to physiologically represent the dendritic excitability.

Interaction of voltage attenuation factors with dendritic excitability

The asymmetry of the dendritic signaling has been quantified by a ratio ($VA_{SD}^{DC}/VA_{DS}^{DC}$) of DC voltage attenuation factors between the soma and a single point in the dendrites [17]. This asymmetry index has been theoretically shown to be proportional
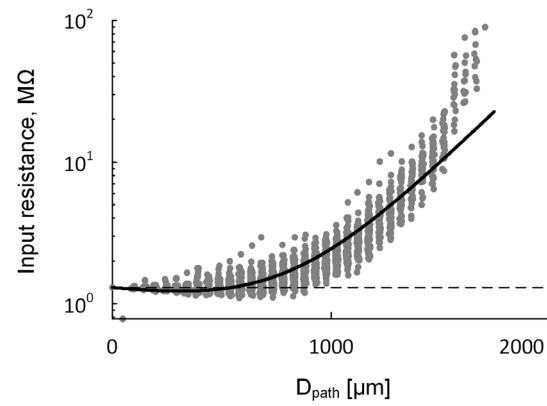
Figure 6. Dependence of input resistance at the dendrites on the DC VA factors. Input resistance ($R_{N,D}$, gray dots) was measured at individual points of the motoneuron dendrites at the same distance with respect to the total current injected to the dendrites (see the stimulation protocol used for the VA_{DS}^{DC}). The measured $R_{N,D}$ was superimposed by the $R_{N,D}$ (black line) that was predicted from fitting curves to the DC VA data using the equation ($R_{N,D}(D_{path}) = R_N*VA_{SD}^{DC}(D_{path})/VA_{DS}^{DC}(D_{path})$) where R_N is input resistance at the soma ($D_{path} = 0$)). Note the agreement between the predicted and measured input resistance in the dendrites. The poor fit at the distal distance was attributed to the error between the VA_{DS}^{DC} data and its fitting curve (see Figure 1(**A**)).
doi:10.1371/journal.pone.0095454.g006

Figure 5. Spatial dependence of cellular excitability on VA_{DS}^{DC} and VA_{SD}^{AC}. All simulation conditions were identical to those used in Figure 4 except for systematically varying the values of the VA_{DS}^{DC} and VA_{SD}^{AC}. Note the inverse order of firing patterns with increasing distance compared to the physiological case (Figure 3). (**A**) – (**D**). F-I$_{soma}$ relationships. (**E**) – (**H**). F-G$_{syn}$ relationships. The direction of black arrows indicates the ascending and descending phase of triangular current stimulation and change in G_{syn}. The gray arrows indicate the current and G_{syn} threshold for activating plateau potentials at different distances from the soma. At different locations, the VA_{DS}^{DC} and VA_{SD}^{AC} were {0.47, 0.6, 0.78, 0.876} and {0.65, 0.31, 0.18, 0.5}. The passive parameter values of the reduced model were $G_{m,S}$={0.228, 0.183, 0.117, 0.067 mS/cm^2}, $G_{m,D}$={0.019, 0.079, 0.181, 0.276 mS/cm^2}, G_C={0.099, 0.135, 0.204, 0.234 mS/cm^2}, $C_{m,S}$={1.644, 1.387, 0.766, 1.617 µF/cm^2}, $C_{m,D}$={0.134, 0.499, 1.373, 0.352 µF/cm^2}. Parameter values in the parentheses are in the order of increasing distance from 200 to 1000 µm. Note that R_N for all reduced models was set to be 1.29 MΩ.
doi:10.1371/journal.pone.0095454.g005

to input resistance ($R_{N,D}$) at the same site of the dendrites leading to the equation [17],

$$R_{N,D}(D_{path}) = R_N \cdot VA_{SD}^{DC}(D_{path})/VA_{DS}^{DC}(D_{path}) \quad (9)$$

where the R_N is assumed to be constant for a single neuron during the variation in the DC VA factors.

In the present study, the VA_{DS}^{DC} was characterized between the soma and all points of the dendrites at the same distance. Our further analysis confirmed that the input resistance predicted with the equation well matched that measured directly from the anatomical model (Figure 6). This result indicates that in the case of 'point-to-all points' the complex distribution of $R_{N,D}$ in the dendrites could also be captured by the same equation as for the case of 'point-to-point'.

It should be first noted that the activation of the PIC may be significantly influenced by both the location and density of the PIC channels in the dendrites. The sensitivity analysis of the PIC activation to individual VA factors was performed at a specific location (i.e. 600 µm) in the dendrites while keeping the density of the PIC channel constant (Figure 4). Our further analysis confirmed the same results at all distances from the soma with the PIC density constant. Under this condition, the influence of the asymmetric signal propagation on the PIC activation in the dendrites may be explained directly from the relationship between the DC VA factors and $R_{N,D}$ in the equation (9).

The equation derived directly from the reduced modeling approach may provide crucial insights into how the asymmetric signal propagation in the dendrites influences the activation threshold for plateau potential and the firing behavior of the neurons. Figure 6 showed that the spatial variation in the input resistance ($R_{N,D}$) of the dendrites was directly related to the spatial variation in the DC VA factors, VA_{SD}^{DC} and VA_{DS}^{DC}. The decrease in the threshold for PIC activation with increasing distance that have been shown during both somatic and dendritic excitation may be explained by the increase in the dendritic input resistance resulting from decrease in VA_{DS}^{DC} as the distance increases (Figure 3). This result was consistent for a broad range of variation in individual voltage attenuation factors at a specific PIC location (Figure 4). The prediction could also be made for Figure 5 taking into account the decreasing $R_{N,D}$ due to the increase in the VA_{DS}^{DC} while holding the VA_{SD}^{DC} in a physiological range. All these results propose the tight relation of the asymmetric signal propagation to the input resistance in the dendrites as a mechanism underlying the influence of the asymmetric signal propagation on the dendritic excitability in motoneurons.

In the present study, the attenuation of AC signals has been considered only for the propagation from the soma to the dendrites assuming the tonic synaptic inputs to the dendrites. The reason for that was not only due to the limitation of the current reduced modeling approach (see Methods), but also the impact of

back-propagating action potentials on the dendritic excitability (compare current threshold for the plateau potential at the dendrites between Figure 2(**G**) and 2(**H**)). The action potentials passively propagating into the dendrites may have both excitatory and inhibitory effects on the activation of PIC channels by their spike and afterhyperpolarization (AHP) phase. The contribution of the passive dendrites to the back-propagation of action potentials was characterized with the VA_{SD}^{AC} which negatively related to the signal frequency. Because the duration of AHP (e.g. 100 ms) is much longer than spike (e.g. 2 ms) in MNs, the inhibitory effect of back-propagating action potentials is expected to be dominant rather than the excitatory effect (compare the current threshold for PIC activation between Figure 2(**G**) and 2(**H**)). This inhibitory effect has been also shown to be important to shape the graded activation of plateau potentials, preventing from being activated in an all-or-none manner [33]. Due to exponential decay of the VA_{SD}^{AC} with increasing distance, the back-propagating action potentials would hamper the activation of PIC channels around the soma more effectively. This implies that the VGICs in proximal dendritic sites would be even harder to be activated relative to distal sites. The similar non-uniformity of dendritic excitability, lower around the soma than distal dendrites, would be expected to occur in other major types of neurons in the brain because they showed the similar profile of the three VA factors as a function of the distance from the soma (Figure 1).

Many computational studies on the nonlinear firing patterns of MNs have suggested that L-type Ca^{2+} channels mediating plateau potentials should be clustered in the dendrites away from the soma to generate the nonlinear firing patterns (hysteretic F-I_{soma} relationship, bottom panel in Figure 2(**H**)) [39,40]. However recent immunohistochemical study has shown the high densities of CaV1.3 clustered at both proximal (<100 μm) and distal sites (450~650 μm) from the soma [41]. Furthermore the nucleated patch clamp recordings from an isolated soma without the dendrites have revealed the existence of Ca PIC channels even at the soma [42]. However, the distal PIC channels may be predominant in determining firing patterns during the current stimulation to the soma because of the higher excitability at the distal dendritic region relative to the proximal sites (Figure 3 and 6).

The location dependent excitability in the dendrites was associated with input/output relationships of the model MN (Figure 3). While varying the location of PIC channels, the MN could reproduce all nonlinear firing patterns experimentally observed in MNs. Four firing types (i.e. Type I-IV) have been classified based on the F-I relationship during triangular current stimulation to the soma [43]. The Type I (linearly overlapping F-I relationship without self-sustained firing) or II firing (clockwise F-I relationship without self-sustained firing) was observed near the soma (<300 μm) whereas the Type III (linearly overlapping F-I relationship with self-sustained firing) or IV (counterclockwise F-I relationship with self-sustained firing) tended to occur in a dendritic region separated further away from the soma (> 600 μm). A variance in firing patterns between MNs might be due to the different distribution of PIC channels in the dendrites, instead of variation in active channel properties.

Variability in voltage attenuation properties and dendritic excitability

The distance dependent VA property of the dendrites is potentially tunable during normal behavior of neural networks. In a MN pool of cat medial gastrocnemius muscle, electrical properties including R_N, τ_m and AHP properties have been reported to be systematically related to the types (S-, FR- and FF-

type) of MNs in a continuous manner [44]. R_N has been shown to have positive effect on the reduction of voltage attenuation by altering the spatial profile of individual VA factors: VA_{SD}^{DC} [21], VA_{SD}^{AC} [18] and VA_{DS}^{DC} (Figure 1(**F**)). The τ_m and AHP properties may further influence the frequency dependent VA_{SD}^{AC} because they are key parameters determining the shape of action potentials. In addition, the membrane electrical properties of individual neurons could be modulated by the different levels of background activity or shunting effect by synapses bombarding the dendritic trees [45,46]. Furthermore the properties of leak current channels determining the cable property might be targeted by a variety of diffusive neurotransmitters to manipulate the spatial dendritic excitability [47,48]. In addition, dendritic morphology is not static, but dynamically varying in physiological conditions. Subtle changes in morphology may also occur due to a various pathological conditions [49-51] or physical damage [52]. All these electrical and morphological changes may influence the VA properties of the dendrites and significantly alter the spatial profile of dendritic excitability, enriching the repertoire of input/output functions of neurons within neural networks without changing physical location or activation properties of VGICs in the dendrites [53,54].

Limitations of the current modeling approach

The asymmetric signal propagation properties of the complex dendrites are implicitly embedded in the anatomically reconstructed neuron models. To explicitly manipulate the asymmetric properties of dendritic signaling and demonstrate their effects on dendritic excitability, we have developed the analytical, two-compartment framework consisting of the somatic and dendritic compartment. In the present study, our previous approach for the asymmetric signal propagation between the soma and a single point in the dendrites has been extended for more natural conditions of the asymmetric signal propagation between the soma and all points in the dendrites at the distance from the soma. For physiological analysis of the role of the asymmetry between the soma and dendrites for dendritic excitability, both passive and active behaviors of the extended model have been validated comparing directly to the input-output properties of its full model with realistic types, kinetics and distribution of voltage-gated ion channels at the soma and dendrites.

However, the fundamental limitations of the two-compartment modeling approach have raised several issues in the present study. The first one is that the collapse of the branching structure of the dendrites into a single compartment sacrificed the details for the activation and deactivation dynamics of PICs positioned at individual branches at the same distance from the soma. Consequently, the PIC (i.e. I_{PIC}) measured at the soma of the anatomical model was more rapidly activated during the rising stimulation phase and more slowly deactivated during the falling stimulation phase compared to the reduced case. In turn, this difference in the rate of I_{PIC} activation and deactivation was the main cause of differences in the I–V (Figure 2(**F**)) and F–I curve (Figure 2(**H**) & (**I**)) between the anatomical and reduced model.

The second is the inability of the two-compartment model to represent the sparse distribution of PIC channels over the dendritic trees. This could limit the production of various types of PIC dynamics experimentally observed such as the staircase PICs [9]. The third one is that the application of the current two-compartment model could be further limited for the case where the distribution of synaptic inputs is not overlapped with that of PICs over a wide area of the dendrites. The second and third limitation of the current reduced modeling approach might be overcome by improving the cable models to incorporate the

physiological properties of the asymmetric signal propagation in the dendrites.

The forth is related to the difference between the new and classic two-compartment modeling approach. Unlike the classic approach where individual model parameters are adjusted as a free parameter to satisfy the characteristic input-output relationship of the real cell [40,55], all cable parameters ($G_{m,S}$, $G_{m,D}$, G_C, $C_{m,S}$ and $C_{m,D}$) of the new approach used in the present study are simultaneously manipulated in a dependent manner to maintain the essential whole cell properties (R_N and τ_m) and signal propagation properties (VA_{SD}^{DC}, VA_{DS}^{DC} and VA_{SD}^{AC}) of the dendrites (see Eq. (4) – (8)). Consequently, the model parameter values of the new model may not be physiologically relevant (e.g. C_m/G_m ratios at each compartment). However, our new approach can provide an analytical framework in which the model parameter values are uniquely determined to retain the biophysical properties that could be experimentally measured from dendritic neurons. In addition, the surface area (or p value in Eq. (5) – (8)) of each compartment in the new model is determined by the location of VGICs in the dendrites allowing for the simulation of varying VGICs in the dendrites based on the physical distance from the soma.

Lastly, the present study was focused on the interplay of plateau potential originated at the dendrites and nonlinear firing behavior of the cells. However, the detail of active conductances underlying the plateau potential was simplified using only L-type Ca channels as previously introduced [29,33]. Thus, the maximum conductance ($G_{Ca,L}$) of the L-type Ca channels may be underestimated in the present study due to the lack of inhibitory VGICs such as calcium dependent potassium currents. Further analysis would be needed for the situation where action potentials (e.g. Na or Ca spikes) are triggered locally at the dendrites, for neurons with somatic input resistances much higher than motoneurons, and for

the morphological conditions that cause the similarity in the voltage attenuation properties in a wide variety of neurons [12].

Implications to reduced modeling of dendritic neurons

The complex dendritic trees have been collapsed into the wide range of levels from multiple equivalent cables to one compartment in many reduced neuron models. The dendritic excitability in the reduced models depends on the reduction methods such as the conservation of surface area [56] or axial resistance [57]. However, it has not been shown to what degree the local excitability in the reduced dendrites is comparable with the anatomical case, resulting in the sacrifice of traceability between the anatomical and reduced models [58]. In the present study, we have shown the close relationship between voltage attenuation factors and dendritic excitability at all distances from the soma (Figure 3 and 6). This finding could provide a theoretical basis for physiologically representing the excitability of the dendrite in the reduced neuron models on the physical domain (i.e. D_{path}), not on the electrical domain (i.e. length constant, λ) used up to date. Thereby the identification of voltage attenuation factors governing spatial heterogeneity of dendritic excitability may bridge the gap between the anatomically reconstructed and reduced neuron models.

Author Contributions

Conceived and designed the experiments: HK CJH KEJ. Performed the experiments: HK. Analyzed the data: HK CJH KEJ. Wrote the paper: HK CJH KEJ.

References

1. London M, Hausser M (2005) Dendritic computation. Annu Rev Neurosci 28: 503–532.
2. Oviedo H, Reyes AD (2005) Variation of input-output properties along the somatodendritic axis of pyramidal neurons. J Neurosci 25: 4985–4995.
3. Gidon A, Segev I (2012) Principles governing the operation of synaptic inhibition in dendrites. Neuron 75: 330–341.
4. Lee RH, Kuo JJ, Jiang MC, Heckman CJ (2003) Influence of active dendritic currents on input-output processing in spinal motoneurons in vivo. J Neurophysiol 89: 27–39.
5. Heckman CJ, Lee RH, Brownstone RM (2003) Hyperexcitable dendrites in motoneurons and their neuromodulatory control during motor behavior. Trends Neurosci 26: 688–695.
6. Rall W (1962) Theory of physiological properties of dendrites. Ann N Y Acad Sci 96: 1071–1092.
7. Bar-Yehuda D, Korngreen A (2008) Space-clamp problems when voltage clamping neurons expressing voltage-gated conductances. J Neurophysiol 99: 1127–1136.
8. Muller W, Lux HD (1993) Analysis of voltage-dependent membrane currents in spatially extended neurons from point-clamp data. J Neurophysiol 69: 241–247.
9. Carlin KP, Bui TV, Dai Y, Brownstone RM (2009) Staircase currents in motoneurons: insight into the spatial arrangement of calcium channels in the dendritic tree. J Neurosci 29: 5343–5353.
10. Mainen ZF, Sejnowski TJ (1996) Influence of dendritic structure on firing pattern in model neocortical neurons. Nature 382: 363–366.
11. Zomorrodi R, Kroger H, Timofeev I (2008) Modeling thalamocortical cell: impact of ca channel distribution and cell geometry on firing pattern. Front Comput Neurosci 2: 5.
12. Hausser M, Spruston N, Stuart GJ (2000) Diversity and dynamics of dendritic signaling. Science 290: 739–744.
13. Segev I, London M (2000) Untangling dendrites with quantitative models. Science 290: 744–750.
14. Rall W, Rinzel J (1973) Branch input resistance and steady attenuation for input to one branch of a dendritic neuron model. Biophys J 13: 648–687.
15. Carnevale NT, Johnston D (1982) Electrophysiological characterization of remote chemical synapses. J Neurophysiol 47: 606–621.
16. Zador AM, Agmon-Snir H, Segev I (1995) The morphoelectrotonic transform: a graphical approach to dendritic function. J Neurosci 15: 1669–1682.
17. Kim H, Jones KE (2011) Asymmetric electrotonic coupling between the soma and dendrites alters the bistable firing behaviour of reduced models. J Comput Neurosci 30: 659–674.
18. Kim H, Jones KE (2012) The retrograde frequency response of passive dendritic trees constrains the nonlinear firing behaviour of a reduced neuron model. PLoS One 7: e43654.
19. Ascoli GA (2006) Mobilizing the base of neuroscience data: the case of neuronal morphologies. Nat Rev Neurosci 7: 318–324.
20. Hines ML, Carnevale NT (1997) The NEURON simulation environment. Neural Comput 9: 1179–1209.
21. Kim H, Major LA, Jones KE (2009) Derivation of cable parameters for a reduced model that retains asymmetric voltage attenuation of reconstructed spinal motor neuron dendrites. J Comput Neurosci 27: 321–336.
22. Cullheim S, Fleshman JW, Glenn LL, Burke RE (1987) Membrane area and dendritic structure in type-identified triceps surae alpha motoneurons. J Comp Neurol 255: 68–81.
23. Fleshman JW, Segev I, Burke RB (1988) Electrotonic architecture of type-identified alpha-motoneurons in the cat spinal cord. J Neurophysiol 60: 60–85.
24. Segev I, Fleshman JW Jr, Burke RE (1990) Computer simulation of group Ia EPSPs using morphologically realistic models of cat alpha-motoneurons. J Neurophysiol 64: 648–660.
25. Holmes WR, Rall W (1992) Electrotonic length estimates in neurons with dendritic tapering or somatic shunt. J Neurophysiol 68: 1421–1437.
26. Thurbon D, Luscher HR, Hofstetter T, Redman SJ (1998) Passive electrical properties of ventral horn neurons in rat spinal cord slices. J Neurophysiol 80: 2485–2502.
27. Major G, Evans JD, Jack JJ (1993) Solutions for transients in arbitrarily branching cables: I. Voltage recording with a somatic shunt. Biophys J 65: 423–449.
28. Coombs JS, Eccles JC, Fatt P (1955) The electrical properties of the motoneurone membrane. J Physiol 130: 291–325.
29. Elbasiouny SM, Bennett DJ, Mushahwar VK (2005) Simulation of dendritic CaV1.3 channels in cat lumbar motoneurons: spatial distribution. J Neurophysiol 94: 3961–3974.
30. Bui TV, Ter-Mikaelian M, Bedrossian D, Rose PK (2006) Computational estimation of the distribution of L-type Ca(2+) channels in motoneurons based

on variable threshold of activation of persistent inward currents. J Neurophysiol 95: 225–241.

31. Hochman S, McCrea DA (1994) Effects of chronic spinalization on ankle extensor motoneurons. II. Motoneuron electrical properties. J Neurophysiol 71: 1468–1479.

32. Lee RH, Heckman CJ (1999) Paradoxical effect of QX-314 on persistent inward currents and bistable behavior in spinal motoneurons in vivo. J Neurophysiol 82: 2518–2527.

33. Elbasiouny SM, Bennett DJ, Mushahwar VK (2006) Simulation of Ca2+ persistent inward currents in spinal motoneurones: mode of activation and integration of synaptic inputs. J Physiol 570: 355–374.

34. Hounsgaard J, Kiehn O (1989) Serotonin-induced bistability of turtle motoneurones caused by a nifedipine-sensitive calcium plateau potential. J Physiol 414: 265–282.

35. Li Y, Bennett DJ (2003) Persistent sodium and calcium currents cause plateau potentials in motoneurons of chronic spinal rats. J Neurophysiol 90: 857–869.

36. Meehan CF, Sukiasyan N, Zhang M, Nielsen JB, Hultborn H (2010) Intrinsic properties of mouse lumbar motoneurons revealed by intracellular recording in vivo. J Neurophysiol 103: 2599–2610.

37. Lee RH, Heckman CJ (1998) Bistability in spinal motoneurons in vivo: systematic variations in persistent inward currents. J Neurophysiol 80: 583–593.

38. Bennett DJ, Hultborn H, Fedirchuk B, Gorassini M (1998) Synaptic activation of plateaus in hindlimb motoneurons of decerebrate cats. J Neurophysiol 80: 2023–2037.

39. Carlin KP, Jones KE, Jiang Z, Jordan LM, Brownstone RM (2000) Dendritic L-type calcium currents in mouse spinal motoneurons: implications for bistability. Eur J Neurosci 12: 1635–1646.

40. Booth V, Rinzel J (1995) A minimal, compartmental model for a dendritic origin of bistability of motoneuron firing patterns. J Comput Neurosci 2: 299–312.

41. Ballou EW, Smith WB, Anelli R, Heckman CJ (2006) Measuring dendritic distribution of membrane proteins. J Neurosci Methods 156: 257–266.

42. Moritz AT, Newkirk G, Powers RK, Binder MD (2007) Facilitation of somatic calcium channels can evoke prolonged tail currents in rat hypoglossal motoneurons. J Neurophysiol 98: 1042–1047.

43. Bennett DJ, Li Y, Siu M (2001) Plateau potentials in sacrocaudal motoneurons of chronic spinal rats, recorded in vitro. J Neurophysiol 86: 1955–1971.

44. Zengel JE, Reid SA, Sypert GW, Munson JB (1985) Membrane electrical properties and prediction of motor-unit type of medial gastrocnemius motoneurons in the cat. J Neurophysiol 53: 1323–1344.

45. Destexhe A, Pare D (1999) Impact of network activity on the integrative properties of neocortical pyramidal neurons in vivo. J Neurophysiol 81: 1531–1547.

46. Williams SR (2004) Spatial compartmentalization and functional impact of conductance in pyramidal neurons. Nat Neurosci 7: 961–967.

47. Goldstein SA, Bockenhauer D, O'Kelly I, Zilberberg N (2001) Potassium leak channels and the KCNK family of two-P-domain subunits. Nat Rev Neurosci 2: 175–184.

48. Nicoll RA, Malenka RC, Kauer JA (1990) Functional comparison of neurotransmitter receptor subtypes in mammalian central nervous system. Physiol Rev 70: 513–565.

49. Yamada M, Wada Y, Tsukagoshi H, Otomo E, Hayakawa M (1988) A quantitative Golgi study of basal dendrites of hippocampal CA1 pyramidal cells in senile dementia of Alzheimer type. J Neurol Neurosurg Psychiatry 51: 1088–1090.

50. Teskey GC, Monfils MH, Silasi G, Kolb B (2006) Neocortical kindling is associated with opposing alterations in dendritic morphology in neocortical layer V and striatum from neocortical layer III. Synapse 59: 1–9.

51. Sousa N, Lukoyanov NV, Madeira MD, Almeida OF, Paula-Barbosa MM (2000) Reorganization of the morphology of hippocampal neurites and synapses after stress-induced damage correlates with behavioral improvement. Neuroscience 97: 253–266.

52. Krenz NR, Weaver LC (1998) Changes in the morphology of sympathetic preganglionic neurons parallel the development of autonomic dysreflexia after spinal cord injury in rats. Neurosci Lett 243: 61–64.

53. van Elburg RA, van Ooyen A (2010) Impact of dendritic size and dendritic topology on burst firing in pyramidal cells. PLoS Comput Biol 6: e1000781.

54. Krichmar JL, Nasuto SJ, Scorcioni R, Washington SD, Ascoli GA (2002) Effects of dendritic morphology on CA3 pyramidal cell electrophysiology: a simulation study. Brain Res 941: 11–28.

55. Pinsky PF, Rinzel J (1994) Intrinsic and network rhythmogenesis in a reduced Traub model for CA3 neurons. J Comput Neurosci 1: 39–60.

56. Clements JD, Redman SJ (1989) Cable properties of cat spinal motoneurones measured by combining voltage clamp, current clamp and intracellular staining. J Physiol 409: 63–87.

57. Bush PC, Sejnowski TJ (1993) Reduced compartmental models of neocortical pyramidal cells. J Neurosci Methods 46: 159–166.

58. Hendrickson EB, Edgerton JR, Jaeger D (2011) The capabilities and limitations of conductance-based compartmental neuron models with reduced branched or unbranched morphologies and active dendrites. J Comput Neurosci 30: 301–321.